

1 Revision 2

2
3 An integrated EPMA-EBSD study of metamorphic histories recorded in
4 garnet

5
6 MASAKI ENAMI^{1,2*}, TAKAYOSHI NAGAYA^{3,4} AND
7 MAW MAW WIN^{3,5}

8
9 ¹ Center for Chronological Research, Nagoya University, Nagoya 464-8602, Japan

10 ² Present address: Institute for Space-Earth Environmental Research, Nagoya University,
11 Nagoya 464-8601, Japan

12 ³ Department of Earth and Planetary Sciences, Graduate School of Environmental
13 Studies, Nagoya University, Nagoya 464-8601, Japan

14 ⁴ Present address: Department of Environmental Studies for Advanced Society,
15 Graduate School of Environmental Studies, Tohoku University, Sendai 980-8579,
16 Japan

17 ⁵ Present address: Yadanabon University, Amarapura, Mandalay, Myanmar

18
19 * E-mail: enami@nagoya-u.jp

20

21

ABSTRACT

22 Growth histories recorded in garnet grains in metasedimentary rocks from the
23 Sanbagawa belt in Japan and the Mogok belt in Myanmar were analyzed using an
24 effective combination of electron backscatter diffraction (EBSD) and electron-probe
25 microanalysis (EPMA) data. Garnet in the Sanbagawa metapelite has inner and outer
26 zones that formed in the eclogite and epidote–amphibolite facies stages, respectively.
27 Based on EPMA element mapping, this garnet appears to have grown as a single crystal
28 with a temporal break in growth between the inner and outer zones that occurred
29 during exhumation. The EBSD data, however, document that the garnet grain is
30 composed of four domains. The misorientation angles of crystallographic orientations
31 between the domains are as large as 59°, and domain boundaries crosscut the growth
32 zoning and the compositional boundary between the inner and outer zones. Sets of
33 quartz grains included in the garnets on either side of the domain boundaries sometimes
34 share the same crystallographic orientation with misorientation angles less than 4°. The
35 garnet grains formed via a 3-step process of prograde crystallization of polycrystalline
36 garnet during the eclogite facies stage (inner zone) resorption around garnet rims and
37 along domain boundaries during exhumation crystallization of the outer zone and in
38 the domain boundaries during the prograde epidote–amphibolite facies stage.

39 The garnet porphyroblasts in the Mogok pelitic gneisses, which formed during
40 prograde metamorphism to the upper amphibolite–granulite facies (0.6–1.0 GPa/780–
41 850°C), are now separated into segments of various sizes by mosaic or symplectite
42 aggregates of biotite, plagioclase, and quartz or monomineralic biotite veins. The
43 segment texture formed at about 0.3–0.4 GPa/610–650°C or lower-grade conditions.
44 The EBSD analysis shows that most of the segments share the same crystallographic

45 orientation with misorientation angles less than 4° and show no evidence of deformation
46 and/or rotation processes after segmentation. These data suggest that the Mogok sample
47 did not experience dynamic deformation of the garnet grains after the resorption and
48 segmentation stage and may have been exhumed under static conditions from depths of
49 9–12 km.

50

51 **Keywords:** EBSD, EPMA, garnet, polycrystals, growth process, metamorphism

52

53

INTRODUCTION

54 Garnet grains serve as an important time capsule by recording the metamorphic
55 evolution of their host rock. Pioneering work by Banno (1965), using electron-probe
56 microanalysis (EPMA), showed compositional heterogeneity of garnet grains in
57 Sanbagawa metapelites and concluded that prograde garnet grains commonly have bell-
58 shaped Mn zoning and are not in complete equilibrium with other matrix phases during
59 prograde metamorphism. Thompson et al. (1977) correlated compositional zoning in
60 garnet with the nature and distribution of its inclusions in the Gassetts schist from
61 Vermont to reveal the paragenetic history of rocks from upper greenschist to lower
62 amphibolite facies conditions. This might have been one of the earliest efforts to exploit
63 the mineralogical characteristics of garnet for interpretation of metamorphic pressure
64 (*P*)–temperature (*T*) paths, and is a concept that has been extensively developed ever
65 since. Moreover, pioneering work by Fliervoet et al. (1997) on deformation mechanisms
66 in ultramylonites from the Redbank Deformed Zone, Central Australia, recognized
67 electron backscatter diffraction (EBSD) as an important tool in the analysis of garnet
68 growth.

69 Garnet generally shows concentric bell-shaped Mn-zoning, which is considered to be
70 formed by nucleation and subsequent continuous growth. Single garnet grains, however,
71 sometimes exhibit multiple regions of high Mn content, which is considered to
72 represent discrete garnet nuclei and their coalescence to form a large porphyroblast (e.g.,
73 Spiess et al. 2001; Okamoto and Michibayashi 2006). In contrast, Hirsch et al. (2003),
74 using EBSD, quantitatively measured the crystallographic orientation of garnet
75 porphyroblasts with multiple domains of Mn-zoning from Harpswell Neck, Maine, and
76 concluded that they exhibited no variation in crystallographic orientation among

77 domains. Thus, a new concept for the growth model of a complex-zoned garnet was
78 proposed in which precursor phases rich in Mn were overgrown, and their Mn was
79 incorporated locally into the garnet structure. The combination of EPMA and EBSD
80 analyses have provided key data for evaluating the growth mechanisms of garnet grains
81 with atoll (Cheng et al. 2007; Ruiz Cruz 2011), snowball (Robyr et al. 2007), and lath
82 shapes (Schertl and Neuser 2007) and for elucidating the interaction between
83 deformation and chemical reaction that occurs during metamorphism (Griffiths et al.
84 2014).

85 Polycrystalline porphyroblasts of garnet with high-angle misorientation boundaries
86 from various types of metamorphic rocks were described by Whitney et al. (2008) and
87 Whitney and Seaton (2010) who determined that the occurrence of polycrystalline
88 garnet porphyroblasts is more frequent than previously believed. Whitney et al. (2008)
89 grouped polycrystalline garnet grains into two types based on Mn growth zoning.
90 Garnet of the first type has concentric compositional zoning of Mn and appears to be a
91 single crystal. The concentric growth zoning of this type of garnet crosscut by high-
92 angle misorientation boundaries. Garnet of the second type has multiple growth nuclei
93 and is identifiably polycrystalline based on both Mn X-ray mapping and EBSD data. In
94 both types of polycrystalline garnet, inclusions of quartz and ilmenite sometimes occur
95 across the domain boundaries. Whitney et al. (2008) determined that the garnet
96 polycrystals formed continuously during the prograde stage and that the differences in
97 compositional zonings can be largely attributed to the spatial distribution of Mn-rich
98 nuclei, i.e., closely or widely spaced nuclei at the early stage of garnet formation [Fig.
99 18 of Whitney et al. (2008)]. Whitney and Seaton (2010) further reported a disconnect
100 between Mn–Fe–Mg zoning and Ca zoning relative to the high-angle misorientation

101 boundaries and proposed the existence of four types of polycrystalline garnet based on
102 the relationships between these two zoning types and high-angle misorientation
103 boundaries [Fig. 11 of Whitney and Seaton (2010)]. These data have prompted
104 important questions in the discussion of metamorphic P - T paths based on the
105 relationships between the zonal structure and inclusions of garnet because the center of
106 a zoned garnet does not always represent the earliest stage of garnet growth. In addition,
107 the misorientation boundaries may behave as channels to promote element exchange
108 between the garnet interior and the matrix phases.

109 Although several important EBSD studies of natural garnet have been conducted,
110 including those listed above, most of these have primarily focused on the growth
111 mechanism of porphyroblasts and deformation processes (e.g., Fliervoet et al. 1997;
112 Prior et al. 2000; Kleinschrodt and Duyster 2002; Storey and Prior 2005; Vollbrecht et
113 al. 2006). Integrated EPMA X-ray mapping and EBSD analysis may also provide
114 important additional information for revealing the P - T - D history. For this study, we
115 selected two samples: one from the high-pressure Sanbagawa metamorphic belt, and the
116 second from the high-temperature Mogok metamorphic belt as case studies to
117 investigate the relationships between the compositional and crystallographic
118 characteristics obtained from EMPA X-ray mapping and EBSD analysis and the
119 implications for the metamorphic P - T - D paths. The Sanbagawa garnet is considered to
120 have experienced discontinuous growth of inner and outer zones based on the
121 compositional zoning and distribution of inclusions. The results of the EBSD analysis
122 revealed that this garnet is composed of four segments and that its high-angle
123 misorientation boundaries crosscut the boundary between the inner and outer zones,
124 which suggests that the polycrystalline texture resulted from multiple nucleations and

125 their coalescence during the early stages of garnet crystallization. The Mogok garnet
126 porphyroblasts were separated into several segments via resorption during exhumation.
127 The EBSD data show no significant misorientation among these segments, which
128 implies static conditions during the later stages of exhumation.

129

130 **GENERAL GEOLOGY OF SAMPLE LOCALITES**

131 The two samples discussed in this paper, UKE07b and S22b, are high-pressure
132 Sanbagawa metamorphic rock from Japan (e.g., Banno and Sakai 1989; Wallis et al.
133 2000) and high-temperature Mogok metamorphic rock from Myanmar (e.g., Searle et al.
134 2007), respectively.

135

136 **Sanbagawa metamorphic rock**

137 The Sanbagawa sample (UKE07b) was collected from the Besshi region of the
138 Sanbagawa metamorphic belt, central Shikoku, Japan, where metapelite and metabasite
139 recrystallized under epidote-amphibolite-facies conditions (Enami 1983;
140 Higashino 1990). Common mineral assemblages of the metapelite and metabasite are
141 garnet + biotite + muscovite + chlorite + sodic-calcic amphibole + epidote + sodic
142 plagioclase + quartz + graphite and sodic-calcic amphibole + garnet + muscovite +
143 epidote + chlorite + sodic plagioclase + quartz, respectively. However, eclogitic
144 assemblages such as garnet + omphacite + quartz occur sporadically in the metabasites
145 (Takasu 1984; Aoya 2001; Kugimiya and Takasu 2002; Ota et al. 2004; Miyagi and
146 Takasu 2005; Sakurai and Takasu 2009; Endo 2010) and rarely in the metapelites
147 (Kouketsu and Enami 2010; Kouketsu et al. 2010) of the high-grade zone. Thus, the
148 Besshi region is divided into eclogite- and non-eclogite units (Kouketsu et al. 2014a).

149 The eclogite-unit lithologies record the relatively complex P – T history of the
150 prograde eclogite facies stage exhumation and hydration stage prograde epidote–
151 amphibolite facies stage (Fig. 1a). On the contrary, the non-eclogite unit lithologies
152 were recrystallized during simple prograde metamorphism up to the epidote–
153 amphibolite facies. These two units are considered to have been juxtaposed after
154 exhumation of the eclogite unit and before the peak stage of the prograde epidote–
155 amphibolite facies metamorphism. The lithologies of the eclogite and non-eclogite units
156 and their boundary were extensively recrystallized under the prograde epidote–
157 amphibolite facies stage. Therefore, it is difficult to directly observe the tectonic
158 boundary between the two units at the outcrop scale; thus the unit boundaries are
159 usually determined on the basis of the following combinations: (1) sodic-phase
160 inclusions in garnet, (2) residual pressure of quartz inclusion in garnet estimated by
161 quartz Raman barometry (Enami et al. 2007; Kouketsu et al. 2014b), and (3)
162 compositional zoning of garnet (e.g., Mouri and Enami 2008; Sakurai and Takasu 2009;
163 Kouketsu et al. 2014a; Taguchi and Enami 2014) in addition to the occurrences of
164 omphacite-bearing assemblages.

165 Endo (2010) proposed a clockwise P – T path for prograde eclogite facies
166 metamorphism and estimated the conditions as 1.9–2.1 GPa/525–565°C and 1.4–1.6
167 GPa/635°C for the peak pressure and temperature stages, respectively. The equilibrium
168 conditions of the peak eclogite facies stage varied slightly from 1.8–1.9 GPa/495–
169 530°C to 2.3–2.4 GPa/675–740°C within the eclogite unit (e.g., Ota et al. 2004;
170 Miyamoto et al. 2007; Kabir and Takasu 2010; Kouketsu et al. 2010; Endo and Tsuboi
171 2013). The P – T conditions in the epidote–amphibolite facies stage of the high-grade
172 zone were estimated to be 0.8–1.1 GPa/470–635°C (Enami 1983; Enami et al. 1994;

173 Wallis et al. 2000).

174

175 **Mogok metamorphic rock**

176 The Mogok sample (S22b) was collected from the Sagaing area of the Mogok
177 metamorphic belt, Myanmar (cf., Fig. 1c of Maw Maw Win et al. 2016). In the Sagaing
178 area, the Mogok metamorphic rocks are composed mainly of pelitic gneiss, marble,
179 calc–silicate rock, and amphibolite of amphibolite–granulite facies grade (Mitchell et al.
180 2007; Maw Maw Win et al. 2016). The pelitic gneiss, which is a predominant lithology
181 in the Sagaing area, is composed mainly of garnet, biotite, plagioclase, K-feldspar,
182 quartz, and graphite. The marble and calc–silicate rocks usually contain phlogopite,
183 diopside, forsterite, grossular garnet, and graphite in addition to calcite. The amphibolite
184 contains mainly hornblende, plagioclase, and epidote with small amounts of biotite and
185 titanite. The petrographical characteristics of the Mogok pelitic gneisses in the Sagaing
186 area and the locality of sample S22b have been described by Maw Maw Win et al.
187 (2016). Pressure–temperature conditions at peak metamorphic stage and exhumation
188 and hydration stage were estimated at 0.6–1.0 GPa/780–850°C and 0.3–0.5 GPa/600–
189 680°C, respectively (Fig. 1b).

190

191 **ANALYTICAL PROCEDURES**

192 Thin sections for X-ray and EBSD mapping analyses and quantitative analyses of
193 major phases were polished by using a series of diamond pastes with decreasing grain
194 sizes down to ¼µm. The X-ray mapping images and the quantitative analyses were
195 conducted by using EPMA with wavelength-dispersive spectrometers (JXA-8900R,
196 JEOL, Tokyo, Japan) at the Petrology Laboratory of Nagoya University. The

197 accelerating voltage and specimen current on Faraday cup were stabilized at 20 kV and
198 100 nA and 15 kV and 12 nA for the X-ray mapping and quantitative analyses,
199 respectively. A beam with a diameter of 2–3 μm was used for the garnet and amphibole
200 analyses; analyses of mica and feldspar were made using a 5 μm beam spot. Well-
201 characterized natural and synthetic phases were used to calibrate the instrument. Matrix
202 corrections were performed using the α -factor table of Kato (2005). Iron in analyzed
203 phases other than epidote was assumed to be ferrous. The compositional characteristics
204 of the garnet are discussed using proportions of end-members estimated as those of
205 divalent cations in the eight coordinated sites; e.g., $\text{Prp} = \text{Mg}/(\text{Fe} + \text{Mn} + \text{Mg} + \text{Ca}) \times$
206 100. Representative analyses of the major minerals in samples UKE07b and S22b are
207 on deposit as Supplemental Table 1¹. The abbreviations for minerals and end-members
208 used in this paper follow those defined by Whitney and Evans (2010).

209 For EBSD analysis, the polished thin sections prepared using diamond pastes were
210 additionally treated with colloidal silica for up to 1 h to remove the surface damage.
211 Crystal orientations were determined at Nagoya University using a JEOL JSM-6510LV
212 scanning electron microscope equipped with a Nordlys Nano detector–AZtec (version
213 2.3) EBSD system at 20 kV accelerating voltage and a working distance of 26–28 mm.
214 The camera binning and Hough resolution were 4×4 and 90, respectively. The
215 maximum (minimum) numbers of band detections were 10 (5). The EBSD patterns
216 were collected under a low vacuum of 10 Pa, which allowed the use of uncoated
217 samples (e.g. Padròn-Navarta et al. 2012; Nagaya et al. 2014). Computerized indexing

¹ Deposit item AM-1X-XXX, Supplemental Table. A deposit item is stored on the MSA web site and available via the American Mineralogist Table of Contents. Find the article in the table of contents at GSW (ammin.geoscienceworld.org) or MSA (www.minsocam.org), and then click on the deposit link.

218 of the diffraction pattern was automatically determined for each measurement. The
219 maximum accepted angular deviation for map measurements was 2.0° . The
220 crystallographic parameters of Novak and Gibbs (1971) and Levien et al. (1980) were
221 employed to index the Kikuchi patterns for garnet, at $a = 11.531 \text{ \AA}$, and for quartz, at a
222 $= 4.916 \text{ \AA}$, $c = 5.4054 \text{ \AA}$, respectively. Software developed by D. Mainprice was used to
223 prepare the pole figures (Mainprice 1990).

224

225 X-RAY MAPPING AND EBSD ANALYSIS

226 UKE07b

227 The UKE07b metapelite was collected from an outcrop 20–30 m inside the
228 northeastern margin of the eclogite unit (longitude $133^\circ 25' 24'' \text{ E}$ and latitude
229 $33^\circ 53' 4'' \text{ N}$). This sample contains garnet, biotite, phengite [Si = 3.30–3.41 per
230 formula unit (pfu) for O = 11], chlorite, epidote [$Y_{\text{Fe}} = \text{Fe}^{3+}/(\text{Al} + \text{Fe}^{3+}) = 0.09\text{--}0.11$],
231 barroisite–katophorite (Si = 6.66–6.70 pfu, Ca = 1.27–1.34 pfu for O = 23), albite, and
232 quartz with minor amounts of rutile, ilmenite, titanite, apatite, and graphite as matrix
233 phases. The biotite was retrogressively altered to secondary chlorite. Paragonite occurs
234 only as inclusions in the garnet. Garnet grains show rounded and subhedral form. Their
235 grain sizes vary from 100–200 μm to 2–3 mm in diameter, and most of them are coarse-
236 grained of $>500 \mu\text{m}$. These relatively coarse garnet grains usually show duplex texture
237 consisting of inner and outer zones identified by the distributions of quartz and graphite
238 inclusions visible under a polarizing microscope.

239 The selected garnet (2.3 mm in size) is also composed of inner and outer zones,
240 visible under the polarizing microscope (Fig. 2a); these results were confirmed by X-
241 ray mapping analyses (Figs. 2b–e). The inner zone is characteristically rich in quartz

242 and fine-grained paragonite, titanite, rutile, and graphite inclusions. The outer zone
243 contains albite rather than paragonite as sodic-phase inclusion. The boundary between
244 the inner and outer zones is also defined by compositional discontinuity (Figs. 2b–f and
245 3). The inner zone is relatively homogeneous ($\text{Alm}_{67-73}\text{Prp}_{4-10}\text{Sps}_{3-10}\text{Grs}_{16-21}$) with
246 slightly decreasing spessartine and increasing pyrope contents from the core toward the
247 margin. The grossular and spessartine contents discontinuously increase, and almandine
248 and pyrope contents discontinuously decrease at the boundary from the inner to outer
249 zones. In the outer zone, the pyrope content increases and the spessartine content
250 decreases toward the outermost rim ($\text{Alm}_{56-66}\text{Prp}_{4-9}\text{Sps}_{0-10}\text{Grs}_{26-36}$). These
251 compositional trends of the inner and outer zones imply prograde formations of these
252 two zones and a discontinuity in garnet growth between the formation stages of the two
253 zones (cf., Fig. 1a). The inner zone contains paragonite and quartz retaining high
254 residual pressure up to 0.6–0.7 GPa, which was thus formed during the eclogite facies
255 stage (cf., Enami et al. 2007; Kouketsu and Enami 2011; Kouketsu et al. 2014a). The
256 outer zone contains albite as inclusions and is a later product than the inner zone,
257 suggesting formation during the epidote–amphibolite facies stage.

258 X-ray mapping analysis revealed concentric zonal structure in the examined garnet
259 grain that appears to have formed from the crystal core toward the rim. The EBSD
260 analysis, however, shows that the grain is polycrystalline, consisting of four domains
261 separated by high-angle misorientation boundaries at 40° – 59° (Figs. 4a and b). These
262 domain boundaries are not related to major element zoning and transect the
263 compositional boundary between the inner and outer zones. Although the quartz
264 inclusions in the garnet grain show no obvious lattice preferred orientation (Figs. 4a and
265 c), those occurring separate from one another across the domain boundaries sometimes

266 share the same crystallographic orientation (Fig. 5). The misorientation angles between
267 quartz inclusions of sets A (grains 1, 2, and 3), B (4, 5, and 6), and C (6 and 7) are less
268 than 5°, 6°, and 2°, respectively.

269

270 **S22b**

271 The S22b pelitic gneiss collected from the Shwe Myin Tin valley (longitude
272 95°59'57" and latitude 22°02'1" N) contains garnet, biotite, plagioclase (An_{43±2}),
273 K-feldspar, and quartz with minor amounts of rutile, ilmenite, graphite, apatite,
274 monazite, and zircon as matrix phases. Biotite grains are characteristically rich in Ti,
275 and their TiO₂ contents are up to 6.2 wt% in phase included by garnet and 4.9 wt% in
276 matrix phase (Ye Kyaw Thu et al. 2016: in press). Sillimanite occurs only as inclusions
277 in the garnet. Garnet grains are anhedral, and some show unusually elongate shapes
278 with aspect ratios up to 1:5 (Figs. 6a–c). The large and elongate garnet grains contain
279 quartz inclusions in their mantle zones showing poikilitic texture. This sample does not
280 show obvious preferred orientation of biotite in the matrix and pressure shadows around
281 the garnet porphyroblasts. The garnet porphyroblasts were retrogressively re-
282 equilibrated under upper greenschist–lower amphibolite facies conditions and are
283 usually separated into several segments by two-types of replacement texture (Maw Maw
284 Win et al. 2016). The earlier re-equilibrium stage is represented by mosaic or
285 symplectite aggregates of biotite, plagioclase, and quartz around the garnet (Figs. 6a, d,
286 and e). The biotite in the aggregates is usually poorer in TiO₂ (usually 1–3 wt%) than
287 the isolated phase in the matrix (up to 4.9 wt%). The later re-equilibrium product is a
288 monomineralic vein of biotite (Fig. 6), which is poorer in TiO₂ (usually less than 0.3
289 wt%) than the isolated phase and the aggregate phase in the matrix.

290 The garnet segments are composed of relatively homogeneous cores ($\text{Alm}_{60-63}\text{Prp}_{29-}$
291 $_{33}\text{Sps}_1\text{Grs}_{5-7}$) and thin Mg-poor and Mn-rich mantles ($\text{Alm}_{63-74}\text{Prp}_{17-29}\text{Sps}_{2-4}\text{Grs}_{4-7}$; Figs.
292 6b–e and 7). In the mantle of grains the pyrope content gradually decreases toward the
293 outermost rim; the almandine and spessartine contents show the opposite trends. The
294 compositional gradient of the mantle part formed along with the segmentation during
295 the retrograde stage, as discussed by Maw Maw Win et al. (2016). Fine-grained garnet
296 sometimes occurs in the aggregates of biotite + plagioclase + quartz and has a chemical
297 composition ($\text{Alm}_{70-78}\text{Prp}_{13-21}\text{Sps}_{2-4}\text{Grs}_{4-7}$) similar to the outermost rim of the garnet.
298 Thus, the Mn-rich garnet + biotite + plagioclase + quartz assemblage likely represents
299 the equilibrium reached when the garnet grains were segmented, as discussed by Maw
300 Maw Win et al. (2016). The local modification in composition of garnet around the
301 monomineralic biotite veins is less extensive than that in the grain mantles (Figs. 6b–e).
302 The anorthite contents of plagioclase are not critically different between the isolated
303 phase in matrix ($\text{An}_{43\pm 2}$) and the aggregate phase ($\text{An}_{41 \pm 4}$).

304 The garnet segments in the area analyzed by EBSD were grouped into three sets of 1–
305 8, 9–12, and 13–15, which are hereafter referred to as garnet sets 1, 2, and 3,
306 respectively (Figs. 8a and d). Garnet sets 1 and 3 contain abundant fine-grained needles
307 of sillimanite, and the garnet set 2 is poor in sillimanite and other inclusions. The
308 differences in the modal amounts of inclusions and the alignment patterns of the
309 sillimanite inclusions imply that the three sets of garnet were likely derived from three
310 different grains (Fig. 6a). The segments of garnet sets 1 and 3 are separated by
311 monomineralic biotite veins except for the cases between segments 1 and 2 and
312 segments 13 and 14, which are bounded by mosaic aggregates of biotite, plagioclase,
313 and quartz. In garnet set 1, the misorientation angles between segments 2 and 8, which

314 are adjacent, are less than 4° ; that misorientation between segments 1 and 2 is 14° (Figs.
315 8a and b). Segments 14 and 15 of garnet set 3, which are bounded by biotite veins, are
316 misoriented by less than 1° , and the misorientation angle between segments 13 and 14 is
317 62° (Figs. 8d and e). Garnet set 2 is composed of four segments separated by mosaic
318 aggregates. Segments 9–11 share similar crystallographic orientations, with
319 misorientation angles of less than 4° ; segment 12 has high-angle misorientation angles
320 of 33° relative to other segments (Figs. 8a and c).

321

322

DISCUSSION

323 **Discontinuous growth of polycrystalline garnets in the Sanbagawa metapelite**

324 Two petrographical characteristics—the relationship between the compositional
325 zoning and domain structure and the crystallographic orientation of quartz inclusions in
326 the garnet—are critical for discussing the growth process of the UKE07b garnet and
327 metamorphic P – T history of the Sanbagawa belt. The Sanbagawa garnet is
328 polycrystalline, and their domain boundaries are developed independent of the
329 compositional growth zoning (Figs. 2b and 4a). This relationship is similar to the case
330 of concentric zoned garnet polycrystals reported by Whitney et al. (2008) and Whitney
331 and Seaton (2010). The Sanbagawa garnet, however, experienced two stages of
332 prograde metamorphism and records the discontinuance of crystal growth between them
333 (Fig. 1a). In addition, the quartz grains included on each side of the garnet domain
334 boundary of the inner zone frequently share similar crystallographic orientation with
335 misorientation angles less than 2 – 6° (Fig. 5). The presence of quartz inclusions sharing
336 similar crystallographic orientation along the domain boundary disproves the
337 interpretation that the polycrystalline garnet and high-angle boundaries were formed by

338 deformation and rotation mechanisms after formation of the porphyroblast. Whitney et
339 al. (2008) studied polycrystalline garnet in mica schist from Townshend Dam and
340 reported that inclusions along the high-angle boundaries in polycrystalline garnet were
341 not offset; thus, they argued that deformation and rotation mechanisms did not cause the
342 formation of the polycrystalline garnet. Our observations suggest that the
343 polycrystalline garnet in sample UKE07b was formed by a process similar to that
344 discussed by Whitney et al. (2008).

345 Higher resolution X-ray element mapping around the domain boundaries (10–20 μm
346 in width) shows local modification of the compositions along the boundaries (Figs. 2c, e,
347 and f). The compositionally modified zone connects to the boundary between the inner
348 and outer zones (Fig. 2f). The compositional ranges of the garnet between the quartz
349 grains (Areas A–C, Figs. 5a and c) and around the domain boundary (Area D, Fig. 5c)
350 are $\text{Alm}_{67-72}\text{Prp}_{5-10}\text{Sps}_{3-6}\text{GrS}_{16-22}$, which are similar to those between the outermost part
351 of the inner zone and the innermost part of the outer zone (Fig. 9). These features
352 suggest the occurrence of two processes: (1) resorption of the garnet's inner zone and
353 quartz inclusions along the domain boundaries by hydration reactions after infiltration
354 of metamorphic fluid during exhumation and a probable temperature decrease and (2)
355 their sealing by neo-crystallization of garnet during the subsequent prograde stage under
356 epidote–amphibolite facies conditions.

357 Figure 10 illustrates conceptual diagrams of the garnet nucleation and growth
358 scenario in the case of the Sanbagawa garnet inferred from the EMPA and EBSD data .
359 Considering that the P – T trajectory of the Sanbagawa eclogite facies rocks have two
360 stages of prograde metamorphism (Fig. 1a), the formation process of the polycrystalline
361 garnet is summarized in the following five processes: (1) formation of closely spaced

362 nuclei of garnet, their coalescence, and trapping of quartz crystals at their domain
363 interface similar to the case of Fig. 18a of Whitney et al. (2008); (2) continuous growth
364 during the prograde eclogite facies stage including the formation of the inner zone
365 containing inclusions of quartz and other phases; (3) resorption around the inner zone of
366 the garnet and along its domain boundaries in the exhumation and hydration stage; (4)
367 resurgence of crystallization and sealing of the domain boundaries at the start of the
368 second prograde metamorphism; and (5) continuous growth of the garnet during the
369 prograde epidote–amphibolite facies stage in the formation of the outer zone.

370

371 **Static exhumation of high-temperature Mogok metamorphic rock**

372 The garnet porphyroblasts in the Mogok metamorphic rocks (S22b) were separated
373 into several segments by mosaic or symplectite aggregates and monomineralic biotite
374 veins. Garnet sets 1 and 3 contain both types of segments bordered by mosaic
375 aggregates and monomineralic veins (Fig. 6). In these garnet sets, the segments
376 separated by monomineralic veins share common crystallographic orientations. On the
377 contrary, segments 1 and 13, which are bordered by mosaic aggregates, show
378 misorientation angles of 14° and 62° to the adjacent segments, respectively (Fig. 8). The
379 high-angle misorientations in segments of sets 1 and 3 might be attributable to two
380 models: (1) primary porphyroblasts with other adjacent segments that were locally
381 rotated after segmentation or (2) independent grains from the other segments that had
382 originally different crystallographic orientations. Although there is little information for
383 discussion of which concept is more plausible, the garnet sets of 1 and 3 (Figs. 8b and
384 e) clearly suggest that the garnet grains did not experience deformation by rotation of
385 these segments after segmentation by monomineralic biotite veins.

386 Segments 9–12 in garnet set 2 are separated by biotite-bearing mosaic aggregates,
387 with segments 9–11 sharing the same crystallographic orientation. On the contrary,
388 segment 12 shows a misorientation angle of 33° to the adjacent segments. No
389 information is available to rule out the possibility that segment 12 originally formed a
390 porphyroblast with segments 9–11 and the high-angle misorientation indicates local
391 rotation of the segment 12 after their segmentation. However, it is highly probable that
392 segments 9-11 did not experience significant rotation and deformation after their
393 separation. These interpretations might be supported by the fact that pelitic gneiss S22b
394 shows no obvious pressure shadow and local overprinting of the foliation around the
395 garnet porphyroblasts.

396 The observation of the sets of garnet segments separated by monomineralic biotite
397 veins, i.e. segments 2–8 and 14–15, certainly suggests that the Mogok sample was static
398 during and after the formation of the veins and not in a strain field. Additionally, the set
399 of segments 9–11, which were separated by biotite-bearing mosaic aggregates, shows
400 that the static environments likely began, at the latest, just before or during the
401 formation stage of the mosaic aggregates. The *P–T* conditions during the formation of
402 the biotite-bearing mosaic or symplectite aggregates in segments 9, 10, and 11 were
403 estimated to be 0.3–0.4 GPa/610–650°C (garnet–biotite–plagioclase–quartz (GBPQ)
404 geobarometry (Wu et al. 2004) and garnet–biotite (Grt–Bt) geothermometry
405 (Bhattacharya et al. 1992; Holdaway 2000)). Such formation conditions of the
406 aggregates are consistent with those of other Mogok pelitic gneisses (0.3–0.5 GPa/600–
407 680°C) reported by Maw Maw Win et al. (2016) and the temperature conditions of
408 about 400–500°C estimated for the garnet isograd in medium P/T type metamorphic
409 belts such as the Barrovian zone (e.g., Spear and Cheney 1989; Spear et al. 1990). The

410 garnet porphyroblasts likely segmented under the lower-amphibolite facies conditions.
411 Although the available data is limited to the studied sample, the Mogok sample S22b
412 may have been exhumed from depths of about 9–12 km, without incurring any specific
413 deformation and rotation,

414

415

IMPLICATIONS

416 The combination of EBSD and EPMA analyses discussed in this paper revealed
417 important information on the geological and tectonic developments of Sanbagawa and
418 Mogok metamorphic rocks along with the growth mechanism of metamorphic garnet
419 grains.

420 **Sanbagawa metapelite:** Two distinct models have been proposed concerning the P –
421 T evolution of the Sanbagawa metamorphic rocks. Aoya (2001), Zaw Win Ko et al.
422 (2005), and Kouketsu et al. (2014a) proposed that the Sanbagawa belt is divided into
423 eclogite and non-eclogite units, and the lithologies of the eclogite unit recording two
424 stages of prograde metamorphism under the eclogite and subsequent epidote–
425 amphibolite facies conditions, as shown in Fig. 1a. As discussed above, this P – T history
426 effectively explains the deduced formation mechanism of the polycrystalline garnet
427 porphyroblast in a Sanbagawa metapelite (UKE07b) from the eclogite unit. On the
428 contrary, Ota et al. (2004) and Aoki et al. (2009) proposed an alternative concept such
429 that eclogite and associated high-grade rocks record simple P – T trajectory with
430 monotonous decreases of P – T conditions during exhumation. They considered that the
431 regional thermal structure up to the epidote–amphibolite facies grade in the Sanbagawa
432 belt is not attributed to progressive metamorphism and instead records Barrovian-type
433 overprinting that occurred during exhumation. However, the proposed simple clockwise

434 *P–T* path model (Ota et al. 2004; Aoki et al. 2009) does not effectively explain the
435 resorption and subsequent crystallization processes during the eclogite facies and
436 epidote–amphibolite facies stages retained by the Sanbagawa garnet.

437

438 **Mogok pelitic gneiss:** The EBSD and EPMA analyses suggested that the Mogok
439 sample S22b did not record any specific deformation and rotation processes under
440 lower-amphibolite facies and lower-grade conditions during exhumation. There may be
441 two possible interpretations for the record of static condition. One is that the degree of
442 deformation, which the Mogok metamorphic belt experienced during later stages of
443 exhumation, was distinctly heterogeneous throughout the Mogok metamorphic belt, and
444 some outcrops, including sample S22b, were thus locally spared from the impact of the
445 exhumation movement.

446 The alternative interpretation is that the Mogok metamorphic belt was almost entirely
447 under static conditions during later stages of exhumation. The Mogok metamorphic
448 rocks may be traced to the north at the eastern Himalayan syntaxis (Barley et al. 2003;
449 Licht et al. 2013). Kaneko (1997) tectonically and petrologically studied the Himalayan
450 metamorphic belt, central Nepal, and proposed a two-step exhumation model of the
451 metamorphic rocks. This model consists of semi-adiabatic extrusion from the Moho
452 depth into the mid-crustal level (about 0.4 GPa/600°C) and subsequent doming uplift
453 along with surface denudation. The static exhumation retained by the Mogok garnet
454 might be explained by the erosion and doming uplift process occurring at depths of at
455 least 10 km and is consistent with the tectonic model proposed by Kaneko (1997).
456 Extensive and systematic studies of the Mogok and/or Himalaya metamorphic belts
457 employing EBSD and EPMA methods possibly provide convincing arguments to the

458 most probable interpretation.

459 The case studies on the Sanbagawa and Mogok metamorphic rocks suggest that the
460 combination of EBSD and EPMA analyses is a powerful and effective method for
461 studies of the P - T - D evolution of metamorphic rocks.

462

463 **ACKNOWLEDGEMENTS**

464 Valuable and constructive comments by D. L. Whitney, T. A. Griffiths and C.
465 Hetherington greatly helped to improve this manuscript. This research was partially
466 supported by Grant-in-Aids for Scientific Research (ME, 25400511; TN, 13J00199)
467 from the Japan Society for the Promotion of Science (JSPS) and a scholarship (MMW)
468 from Ministry of Education, Culture, Sports, Science and Technology in Japan (MEXT).
469

470

REFERENCES CITED

- 471 Aoki, K., Kitajima, K., Masago, H., Nishizawa, M., Terabayashi, M., Omori, S.,
472 Yokoyama, T., Takahata, N., Sano, Y., and Maruyama, S. (2009) Metamorphic P–
473 T–time history of the Sanbagawa Belt in central Shikoku, Japan and implications
474 for retrograde metamorphism during exhumation. *Lithos*, 113, 393-407.
- 475 Aoya, M. (2001) P–T–D path of eclogite from the Sambagawa belt deduced from
476 combination of petrological and microstructural analyses. *Journal of Petrology*, 42,
477 1225-1248.
- 478 Banno, S. (1965) Notes on rock-forming minerals (34) Zonal structure of pyralspite
479 garnet in Sanbagawa schists in the Bessi area, Sikoku. *Journal of Geological*
480 *Society of Japan*, 71, 185-188.
- 481 Banno, S. and Sakai, C. (1989) Geology and metamorphic evolution of the Sanbagawa
482 metamorphic belt, Japan. In J.S. Daly, R.A. Cliff, and B.W.D. Yardley Eds., *The*
483 *Evolution of Metamorphic Belts*, 43, p. 519-532. Blackwell Scientific
484 Publications, Oxford.
- 485 Barley, M.E., Pickard, A.L., Khin Zaw, Rak, P., and Doyle, M.G. (2003) Jurassic to
486 Miocene magmatism and metamorphism in the Mogok metamorphic belt and the
487 India-Eurasia collision in Myanmar. *Tectonics*, 22.
- 488 Bhattacharya, A., Mohanty, L., Maji, A., Sen, S.K., and Raith, M. (1992) Non-ideal
489 mixing in the phlogopite-annite binary: constraints from experimental data on
490 Mg-Fe partitioning and a reformulation of the biotite-garnet geothermometer.
491 *Contributions to Mineralogy and Petrology*, 111, 87-93.
- 492 Cheng, H., Nakamura, E., Kobayashi, K., and Zhou, Z. (2007) Origin of atoll garnets in
493 eclogites and implications for the redistribution of trace elements during slab

- 494 exhumation in a continental subduction zone. *American Mineralogist*, 92, 1119-
495 1129.
- 496 Enami, M. (1983) Petrology of pelitic schists in the oligoclase-biotite zone of the
497 Sanbagawa metamorphic terrain, Japan: phase equilibria in the highest grade zone
498 of a high-pressure intermediate type of metamorphic belt. *Journal of*
499 *Metamorphic Geology*, 1, 141-161.
- 500 Enami, M., Nishiyama, T., and Mouri, T. (2007) Laser Raman microspectrometry of
501 metamorphic quartz: A simple method for comparison of metamorphic pressures.
502 *American Mineralogist*, 92, 1303-1315.
- 503 Enami, M., Wallis, S.R., and Banno, Y. (1994) Paragenesis of sodic pyroxene-bearing
504 quartz schists: implications for the P-T history of the Sanbagawa belt.
505 *Contributions to Mineralogy and Petrology*, 116, 182-198.
- 506 Endo, S. (2010) Pressure-temperature history of titanite-bearing eclogite from the
507 Western Iratsu body, Sanbagawa metamorphic belt, Japan. *Island Arc*, 19, 313-
508 335.
- 509 Endo, S., and Tsuboi, M. (2013) Petrogenesis and implications of jadeite-bearing
510 kyanite eclogite from the Sanbagawa belt (SW Japan). *Journal of Metamorphic*
511 *Geology*, 31, 647-661.
- 512 Fliervoet, T.F., White, S.H., and Drury, M.R. (1997) Evidence for dominant grain-
513 boundary sliding deformation in greenschist- and amphibolite-grade
514 polymineralic ultramytonites from the Redbank Deformed Zone, Central
515 Australia. *Journal of Structural Geology*, 19, 1495-1520.
- 516 Griffiths, T.A., Habler, G., Rhede, D., Wirth, R., Ram, F., and Abart, R. (2014)
517 Localization of submicron inclusion re-equilibration at healed fractures in host

- 518 garnet. *Contributions to Mineralogy and Petrology*, 168.
- 519 Higashino, T. (1990) The higher-grade metamorphic zonation of the Sambagawa
520 metamorphic belt in central Shikoku, Japan. *Journal of Metamorphic Geology*, 8,
521 413-423.
- 522 Hirsch, D.M., Prior, D.J., and Carlson, W.D. (2003) An overgrowth model to explain
523 multiple, dispersed high-Mn regions in the cores of garnet porphyroblasts.
524 *American Mineralogist*, 88, 131-141.
- 525 Holdaway, M.J. (2000) Application of new experimental and garnet Margules data to
526 the garnet-biotite geothermometer. *American Mineralogist*, 85, 881-892.
- 527 Kaneko, Y. (1997) Two-step exhumation model of the Himalayan metamorphic belt,
528 central Nepal. *Journal of Geological Society of Japan*, 103, 203-226.
- 529 Kabir, M.F. and Takasu, A. (2010) Evidence for multiple burial–partial exhumation
530 cycles from the Onodani eclogites in the Sambagawa metamorphic belt, central
531 Shikoku, Japan. *Journal of Metamorphic Geology*, 28, 873-893.
- 532 Kato, T. (2005) New accurate Bence-Albee α -factors for oxides and silicates calculated
533 from the PAP correction procedure. *Geostandards and Geoanalytical Research*, 29,
534 83-94.
- 535 Kleinschrodt, R., and Duyster, J.P. (2002) HT-deformation of garnet: an EBSD study on
536 granulites from Sri Lanka, India and the Ivrea Zone. *Journal of Structural
537 Geology*, 24, 1829-1844.
- 538 Kouketsu, Y., and Enami, M. (2010) Aragonite and omphacite-bearing metapelite from
539 Besshi region, Sambagawa belt in central Shikoku, Japan and its implication.
540 *Island Arc*, 19, 165-176.
- 541 Kouketsu, Y., and Enami, M. (2011) Calculated stabilities of sodic phases in the

- 542 Sambagawa metapelites and their implications. *Journal of Metamorphic Geology*,
543 29, 301-316.
- 544 Kouketsu, Y., Enami, M., and Mizukami, T. (2010) Omphacite-bearing metapelite from
545 the Besshi region, Sambagawa metamorphic belt, Japan: Prograde eclogite facies
546 metamorphism recorded in metasediment. *Journal of Mineralogical and*
547 *Petrological Sciences*, 105, 9-19.
- 548 Kouketsu, Y., Enami, M., Mouri, T., Okamura, M., and Sakurai, T. (2014a) Composite
549 metamorphic history recorded in garnet porphyroblasts of Sambagawa
550 metasediments in the Besshi region, central Shikoku, Southwest Japan. *Island Arc*,
551 23, 263-280.
- 552 Kouketsu, Y., Nishiyama, T., Ikeda, T., and Enami, M. (2014b) Evaluation of residual
553 pressure in host-inclusion system using the negative frequency shift of quartz
554 Raman spectrum. *American Mineralogist*, 99, 433-442.
- 555 Kugimiya, Y., and Takasu, A. (2002) Geology of the Western Iratsu mass within the
556 tectonic melange zone in the Sambagawa metamorphic belt, Besshi district,
557 central Shikoku, Japan. *Journal of Geological Society of Japan*, 108, 644-662 (in
558 Japanese with English abstract).
- 559 Levien, L., Prewitt, C.T., and Weidner, D.J. (1980) Structure and elastic properties of
560 quartz at pressure. *American Mineralogist*, 65, 920-930.
- 561 Licht, A., France-Lanord, C., Reisberg, L., Fontaine, C., Soe, A.N., and Jaeger, J.J.
562 (2013) A palaeo Tibet-Myanmar connection? Reconstructing the Late Eocene
563 drainage system of central Myanmar using a multi-proxy approach. *Journal of*
564 *Geological Society, London*, 170, 929-939.
- 565 Mainprice, D.A. (1990) Fortran program to calculate seismic anisotropy from the lattice

- 566 preferred orientation of minerals. *Computers & Geosciences*, 16, 385-393.
- 567 Maw Maw Win, Enami, M., and Kato, T. (2016) Metamorphic conditions and CHIME
568 monazite ages of Late Eocene to Late Oligocene high-temperature Mogok
569 metamorphic rocks in central Myanmar. *Journal of Asian Earth Sciences*, 117,
570 304-316.
- 571 Mitchell, A.H.G., Myint Thein Htay, Htun, K.M., Myint Naing Win, Thura Oo, and Tin
572 Hlaing. (2007) Rock relationships in the Mogok metamorphic belt, Tatkon to
573 Mandalay, central Myanmar. *Journal of Asian Earth Sciences*, 29, 891-910.
- 574 Miyagi, Y., and Takasu, A. (2005) Prograde eclogites from the Tonaru epidote
575 amphibolite mass in the Sambagawa Metamorphic Belt, central Shikoku,
576 southwest Japan. *Island Arc*, 14, 215-235.
- 577 Miyamoto, A., Enami, M., Tsuboi, M., and Yokoyama, K. (2007) Peak conditions of
578 kyanite-bearing quartz eclogites in the Sanbagawa metamorphic belt, central
579 Shikoku, Japan. *Journal of Mineralogical and Petrological Sciences*, 102, 352-367.
- 580 Mouri, T. and Enami, M. (2008) Areal extent of eclogite facies metamorphism in the
581 Sanbagawa belt, Japan: New evidence from a Raman microprobe study of quartz
582 residual pressure. *Geology*, 36, 503-506.
- 583 Nagaya, T., Wallis, S.R., Kobayashi, H., Michibayashi, K., Mizukami, T., Seto, Y.,
584 Miyake, A., and Matsumoto, M. (2014) Dehydration breakdown of antigorite and
585 the formation of B-type olivine CPO. *Earth and Planetary Science Letters*, 387,
586 67-76.
- 587 Novak, G.A., and Gibbs, G.V. (1971) The crystal chemistry of the silicate garnets.
588 *American Mineralogist*, 56, 791-825.
- 589 Okamoto, A., and Michibayashi, K. (2006) Misorientations of garnet aggregate within a

- 590 vein; an example from the Sanbagawa metamorphic belt, Japan. *Journal of*
591 *Metamorphic Geology*, 24, 353-366.
- 592 Ota, T., Terabayashi, M., and Katayama, I. (2004) Thermobaric structure and
593 metamorphic evolution of the Iratsu eclogite body in the Sanbagawa belt, central
594 Shikoku, Japan. *Lithos*, 73, 95-126.
- 595 Padròn-Navarta, J.A., Tommasi, A., Garrido, C.J., and Sánchez-Vizcaíno, V.L. (2012)
596 Plastic deformation and development of antigorite crystal preferred orientation in
597 high-pressure serpentinites. *Earth and Planetary Science Letters*, 349-350, 75-86.
- 598 Pattison, D.R.M. (2001) Instability of Al₂SiO₅ “triple-point” assemblages in
599 muscovite+biotite+quartz-bearing metapelites, with implications. *American*
600 *Mineralogist*, 86, 1414-1422.
- 601 Prior, D.J., Wheeler, J., Brenker, F.E., Harte, B., and Matthews, M. (2000) Crystal
602 plasticity of natural garnets: new microstructural evidence. *Geology*, 28, 1003-
603 1006.
- 604 Robyr, M., Vonlanthen, P., Baumgartner, L.P., and Grobet, B. (2007) Growth
605 mechanism of snowball garnets from the Lukmanier Pass area (Central Alps,
606 Switzerland): a combined μ CT/EPMA/EBSD study. *Terra Nova*, 19, 240-244.
- 607 Ruiz Cruz, M.D. (2011) Origin of atoll garnet in schists from the Alpujarride Complex
608 (Central zone of the Betic Cordillera, Spain): Implications on the P-T evolution.
609 *Mineralogy and Petrology*, 101, 245-261.
- 610 Sakurai, T., and Takasu, A. (2009) Geology and metamorphism of the Gazo mass
611 (eclogite-bearing tectonic block) in the Sambagawa metamorphic belt, Besshi
612 district, central Shikoku, Japan. *Journal of Geological Society of Japan*, 115, 101-
613 121 (in Japanese with English abstract).

- 614 Schertl, H.P., and Neuser, R.D. (2007) Unusual lath-shaped garnet-zoisite intergrowth
615 textures from a UHP zoisite-quartz fels, Dora Maira, northwest Italy: An EBSD
616 case study. *International Geology Review*, 49, 626-635.
- 617 Searle, M.P., Noble, S.R., Cottle, J.M., Waters, D.J., Mitchell, A.H.G., Tin Hlaing, and
618 Horstwood, M.S.A. (2007) Tectonic evolution of the Mogok metamorphic belt,
619 Burma (Myanmar) constrained by U-Th-Pb dating of metamorphic and magmatic
620 rocks. *Tectonics*, 26, TC3014.
- 621 Spear, F.S. and Cheney, J.T. (1989) A petrogenetic grid for pelitic schists in the system
622 $\text{SiO}_2\text{-Al}_2\text{O}_3\text{-FeO-MgO-K}_2\text{O-Na}_2\text{O-H}_2\text{O}$. *Contributions to Mineralogy and*
623 *Petrology*, 101, 149-164.
- 624 Spear, F.S., Kohn, M.J., Florence, F.P., and Menard, T. (1990) A model for garnet and
625 plagioclase growth in pelitic schists; implications for thermobarometry and P-T
626 path determinations. *Journal of Metamorphic Geology*, 8, 683-696.
- 627 Spiess, R., Peruzzo, L., Prior, D.J., and Wheeler, J. (2001) Development of garnet
628 porphyroblasts by multiple nucleation, coalescence and boundary misorientation-
629 driven rotations. *Journal of Metamorphic Geology*, 19, 269-290.
- 630 Storey, C.D., and Prior, D.J. (2005) Plastic deformation and recrystallization of garnet:
631 A mechanism to facilitate diffusion creep. *Journal of Petrology*, 46, 2593-1613.
- 632 Taguchi, T., and Enami, M. (2014) Compositional zoning and inclusions of garnet in
633 Sanbagawa metapelites from the Asemi-gawa route, central Shikoku, Japan.
634 *Journal of Mineralogical and Petrological Sciences*, 109, 1-12.
- 635 Takasu, A. (1984) Prograde and retrograde eclogites in the Sambagawa metamorphic
636 belt, Besshi district, Japan. *Journal of Petrology*, 25, 619-643.
- 637 Thompson, A.B., Tracy, R.J., Lyttle, P., and Thompson, J.B.J. (1977) Prograde reaction

- 638 histories deduced from compositional zonation and mineral inclusions in garnet
639 from the Gassetts schist, Vermont. *American Journal of Science*, 277, 1152-1167.
- 640 Vollbrecht, A., Pawlowski, J., Leiss, B., Heinrichs, T., Seidel, M., and Kronz, A. (2006)
641 Ductile deformation of garnet in mylonitic gneisses from the Munchberg Massif
642 (Germany). *Tectonophysics*, 427, 153-170.
- 643 Wallis, S., Takasu, A., Enami, M., and Tsujimori, T. (2000) Eclogite and related
644 metamorphism in the Sanbagawa belt, Southwest Japan. *Bulletin of Research*
645 *Institute of Natural Sciences, Okayama University of Science*, 26, 3-17.
- 646 Whitney, D.L., and Evans, B.W. (2010) Abbreviations for names of rock-forming
647 minerals. *American Mineralogist*, 95, 185-187.
- 648 Whitney, D.L., Goergen, E.T., Ketcham, R.A., and Kunze, K. (2008) Formation of
649 garnet polycrystals during metamorphic crystallization. *Journal of Metamorphic*
650 *Geology*, 26, 365-383.
- 651 Whitney, D.L. and Seaton, N.C.A. (2010) Garnet polycrystals and the significance of
652 clustered crystallization. *Contributions to Mineralogy and Petrology*, 160, 591-
653 607.
- 654 Wu, C.-M., Zhang, J., and Ren, L.-D. (2004) Empirical garnet-biotite-plagioclase-
655 quartz (GBPQ) geobarometry in medium- to high-grade metapelites. *Journal of*
656 *Petrology*, 45, 1907-1921.
- 657 Ye Kyaw Thu, Maw Maw Win, Enami, M., and Tsuboi, M. (2016: in press) Ti-rich
658 biotite in spinel and quartz-bearing paragneiss and related rocks from the Mogok
659 metamorphic belt, central Myanmar. *Journal of Mineralogical and Petrological*
660 *Sciences*, 111, doi: 10.2465/jmps.151020.
- 661

- 662 Zaw Win Ko, Enami, M., and Aoya, M. (2005) Chloritoid and barroisite-bearing pelitic
663 schists from the eclogite unit in the Besshi district, Sanbagawa metamorphic belt.
664 Lithos, 81, 79-100.
665

666 Figure captions

667 FIGURE 1. (a) Schematic diagram showing the pressure–temperature paths of
668 composite- and normal-zoned garnets in metapelites collected from eclogite and
669 non-eclogite units of the Besshi region in the Sanbagawa belt [partly modified
670 from Fig. 11b of Kouketsu et al. (2014a)]. (b) Pressure and temperature
671 estimations of the Mogok metamorphic rocks from the Sagaing area, central
672 Myanmar. Abbreviations are: And, andalusite; Ky, kyanite; Sil, sillimanite; M16,
673 Maw Maw Win (2016). Stability ranges of aluminum silicates are from Pattison
674 (2001).

675 FIGURE 2. (a) Photomicrograph and (b) CaK α , (c) MgK α , (d) FeK α , and (e) and (f)
676 MnK α X-ray mapping images of a garnet in the Sanbagawa metapelite sample
677 (UKE07b). In the X-ray mapping images, warmer colors indicate high
678 concentrations of elements. The white lines in Fig. 2b correspond to the domain
679 boundaries shown in Fig. 4a determined by EBSD analysis, and that in Fig. 2e
680 indicates outline of garnet. Line A–B indicates the position of the step-scan
681 analysis shown in Fig. 3.

682 FIGURE 3. Step-scan analysis of a garnet in the Sanbagawa metapelite sample
683 (UKE07b). The position of the step-scan is shown in Fig. 2a. Abbreviations for
684 end-members: Alm: almandine; Grs: grossular; Prp: pyrope; Sps: spessartine.

685 FIGURE 4. Four-domain garnet polycrystals containing quartz inclusions in the
686 Sanbagawa metapelite sample (UKE07b). (a) Electron backscatter diffraction
687 (EBSD) map (6 μ m grid step) showing the relationships of crystallographic
688 orientations of garnet domains and quartz inclusions. Average crystallographic
689 orientations of quartz inclusions are indicated by colored circles corresponding to

690 the Euler angle color key. (b) Equal-area and lower hemisphere projection
691 showing average crystallographic orientations of garnet domains. The Euler angle
692 color keys and band contrast are shown in (a). (c) Equal-area and lower
693 hemisphere projections showing average crystallographic orientations of quartz
694 grains included in the garnet shown in (a). The Euler angle color keys of the poles
695 are the same as those of the quartz inclusions shown in (a).

696 FIGURE 5. Relationships of crystallographic orientations of sets of quartz grains [(1)–
697 (3), (4)–(5), and (6)–(7)] included in the neighboring garnet domains in the
698 Sanbagawa metapelite sample (UKE07b) shown in Fig. 4a. (a) and (c) Electron
699 backscatter diffraction (EBSD) maps (1 μm grid step) of quartz inclusions and
700 host garnet. The mapped areas are shown in Figs. 2f and 4a. The different colors,
701 which correspond to the Euler angle color key, denote different orientations of
702 quartz and garnet. (b) and (d) Equal-area and lower hemisphere projections
703 showing average crystallographic orientations of quartz grains. The Euler angle
704 color keys of (b) and (d) are shown in (a) and (c), respectively. Areas A–D are
705 domain boundaries analyzed by EPMA; their compositions are shown in Fig. 9.
706 Abbreviations for minerals: Grt, garnet; Qz, quartz.

707 FIGURE 6. (a) Photomicrograph, (b) and (d) MgK α , and (c) and (e) MnK α X-ray
708 images of sets of garnet segments in the Mogok pelitic gneiss sample (S22b). In
709 the X-ray map images, warmer colors indicate high concentrations of elements.
710 Line C–D indicates the position of the step-scan analysis shown in Fig. 7.
711 Abbreviations for minerals: Bt: biotite; Grt: garnet; Pl: plagioclase; Qz: quartz.

712 FIGURE 7. Step-scan analysis of a garnet in the Mogok pelitic gneiss sample (S22b).
713 The position of the step-scan is shown in Fig. 6a. Abbreviations for end-members:

714 Alm: almandine; Grs: grossular; Prp: pyrope; Sps: spessartine.

715 FIGURE 8. Sets of garnet segments in the Mogok pelitic gneiss sample (S22b). (a) and
716 (d) Electron backscatter diffraction (EBSD) maps (10 μm grid step) showing
717 similarities and differences in the lattice orientations of the garnet segments.
718 Different colors denote different orientations. (b), (c), and (e) Equal-area and
719 lower hemisphere projections showing average crystallographic orientations of all
720 segments in each figure.

721 FIGURE 9. Compositional variations of a garnet in the Sanbagawa metapelite sample
722 (UKE07b). The positions of areas A–D of the segment boundary are shown in
723 Figs. 5a and c.

724 FIGURE 10. Conceptual diagram of the garnet nucleation and growth scenario of garnet
725 polycrystals in the Sanbagawa metapelite (UKE07b). The growth of this grain
726 began in the initial formations of closely spaced nuclei followed by their
727 coalescence during the early stage of prograde eclogite facies metamorphism. At
728 that time, some of the quartz grains were included at the domain boundaries.

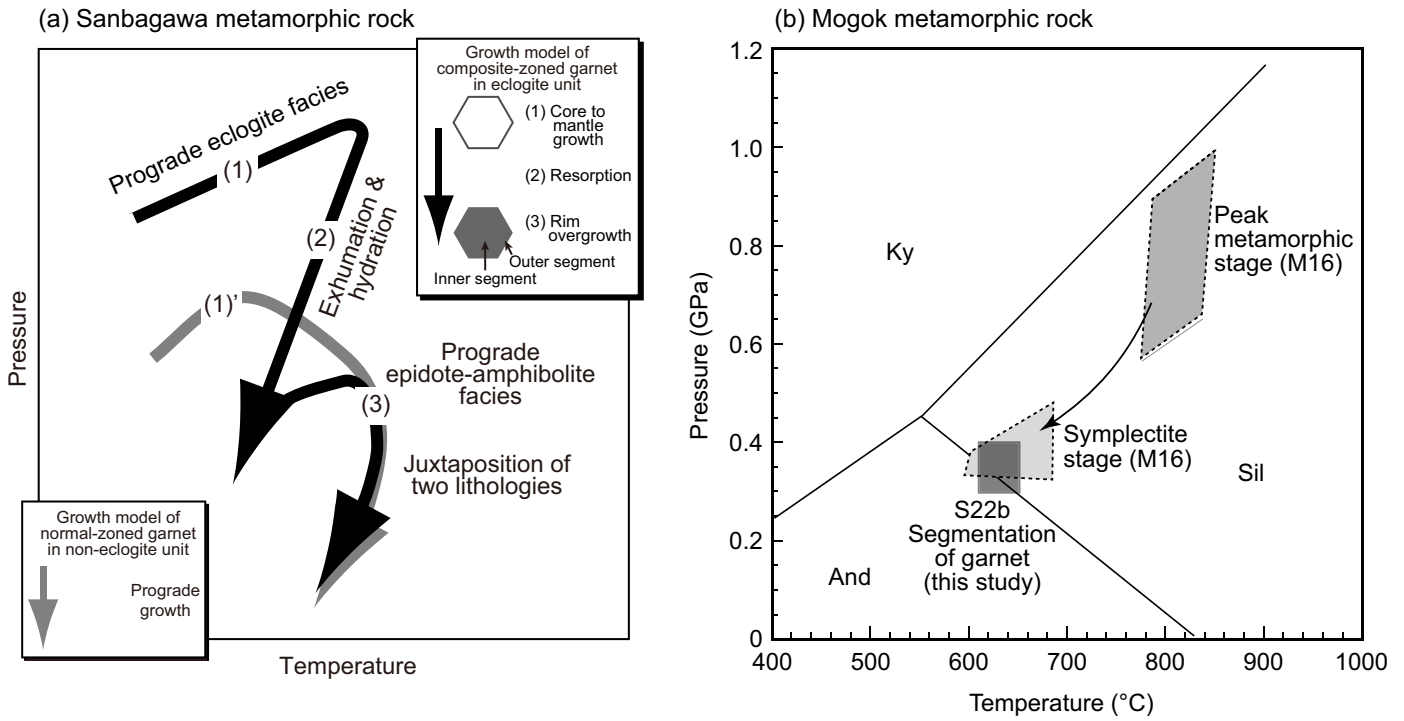


Figure 01 (Enami and others)

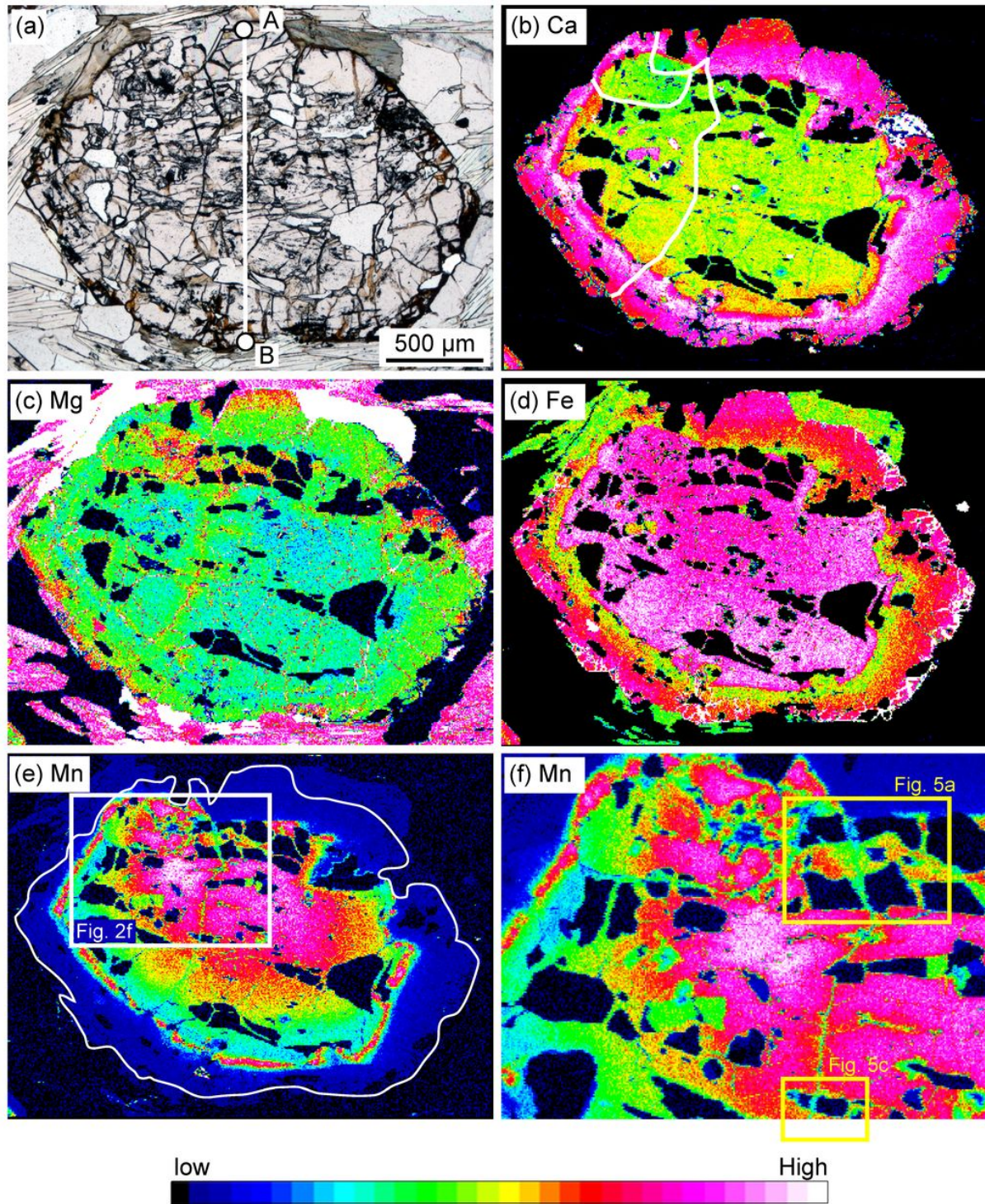


Figure 02 (Enami and others)

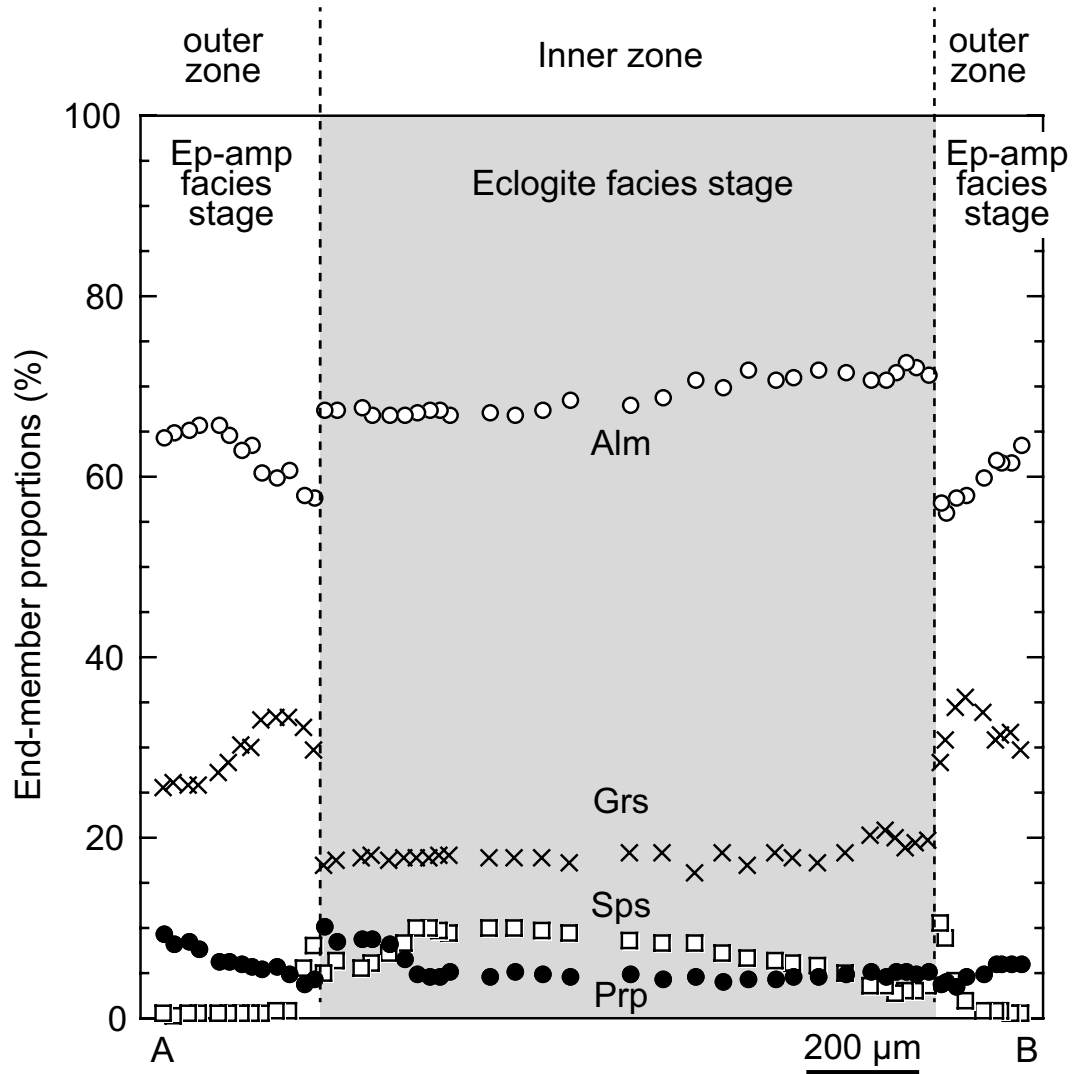
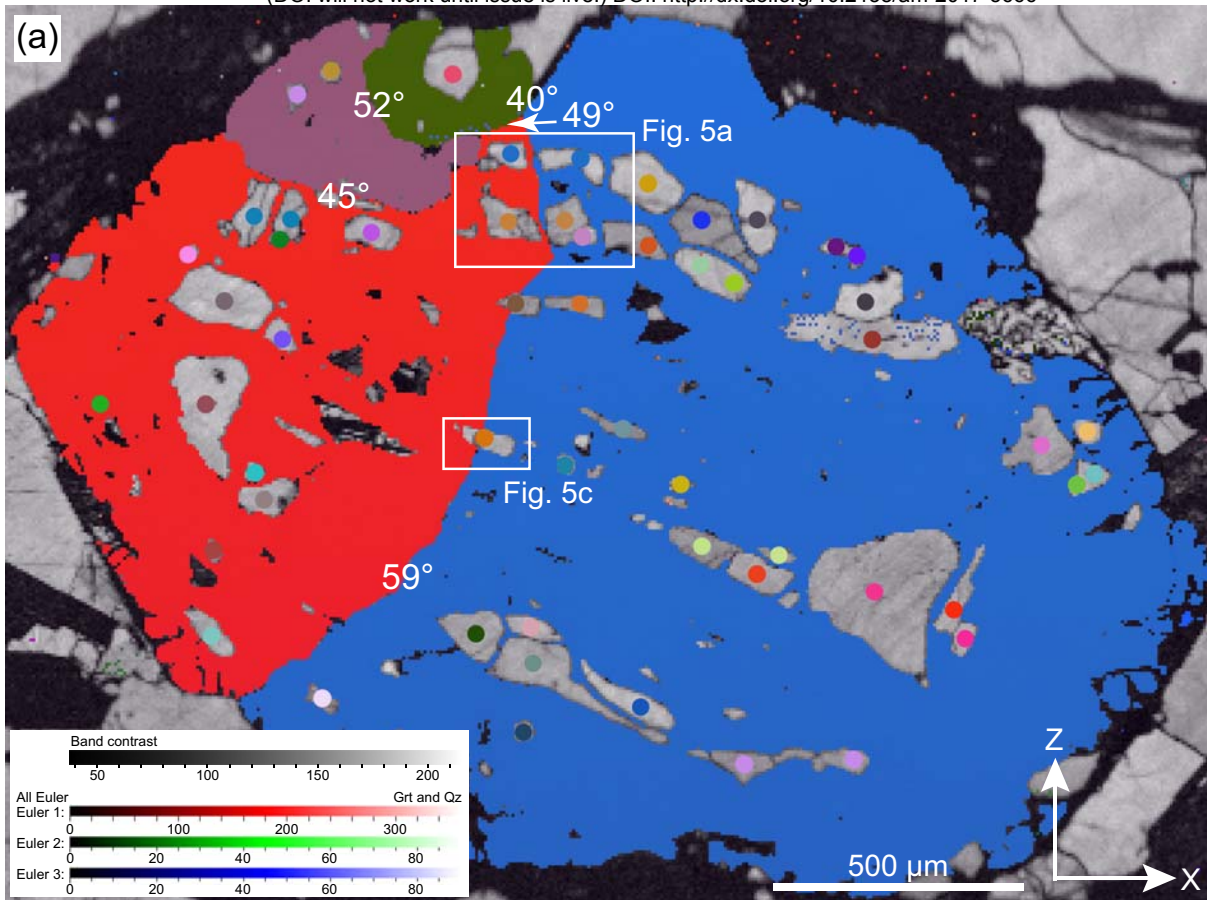
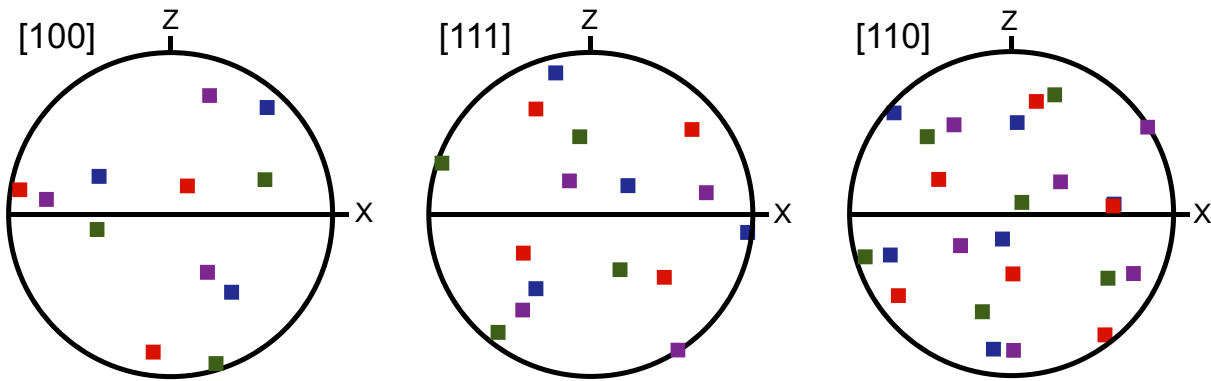


Figure 03 (Enami and others9)



(b) Garnet



(c) Quartz

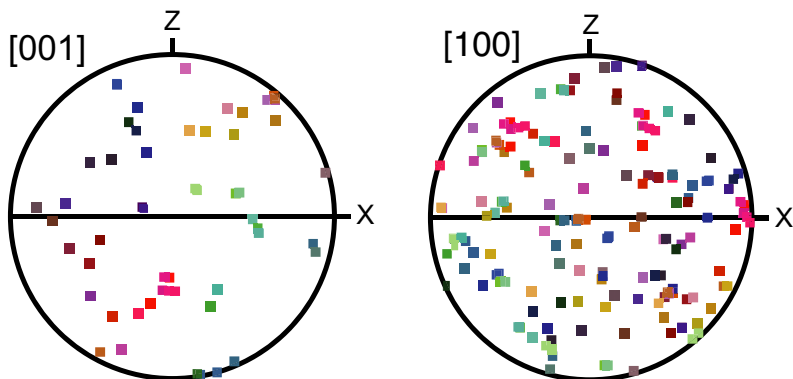


Figure 04 (Enami and others)

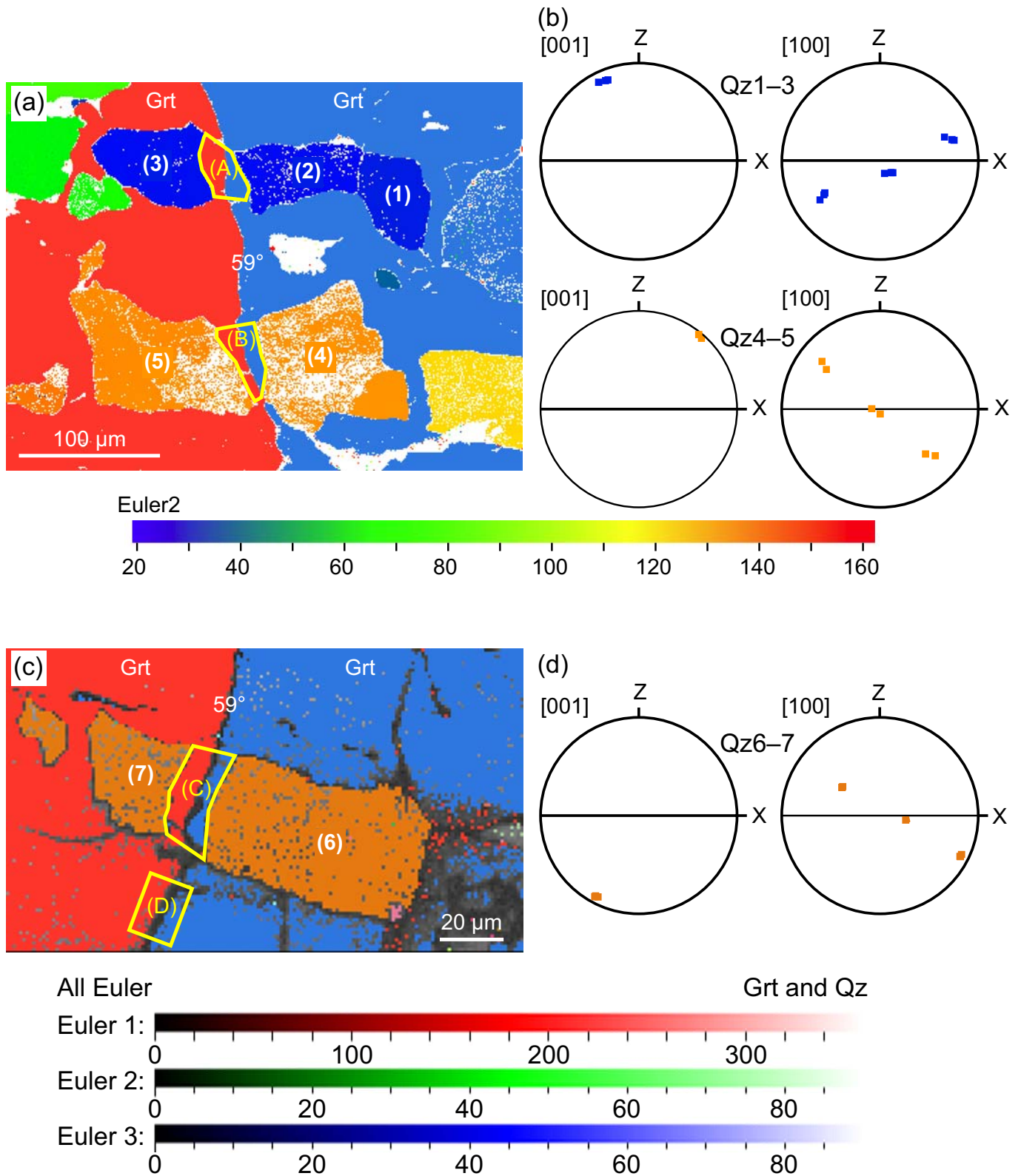


Figure 05 (Enami and others)

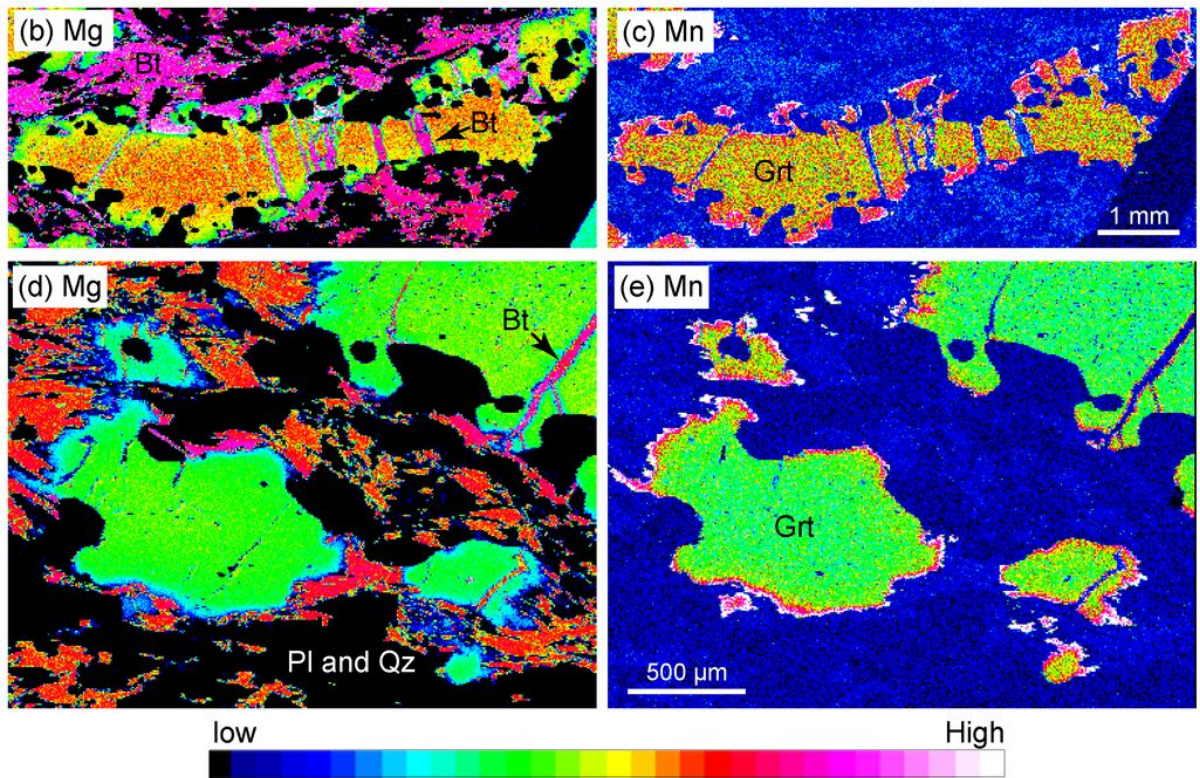
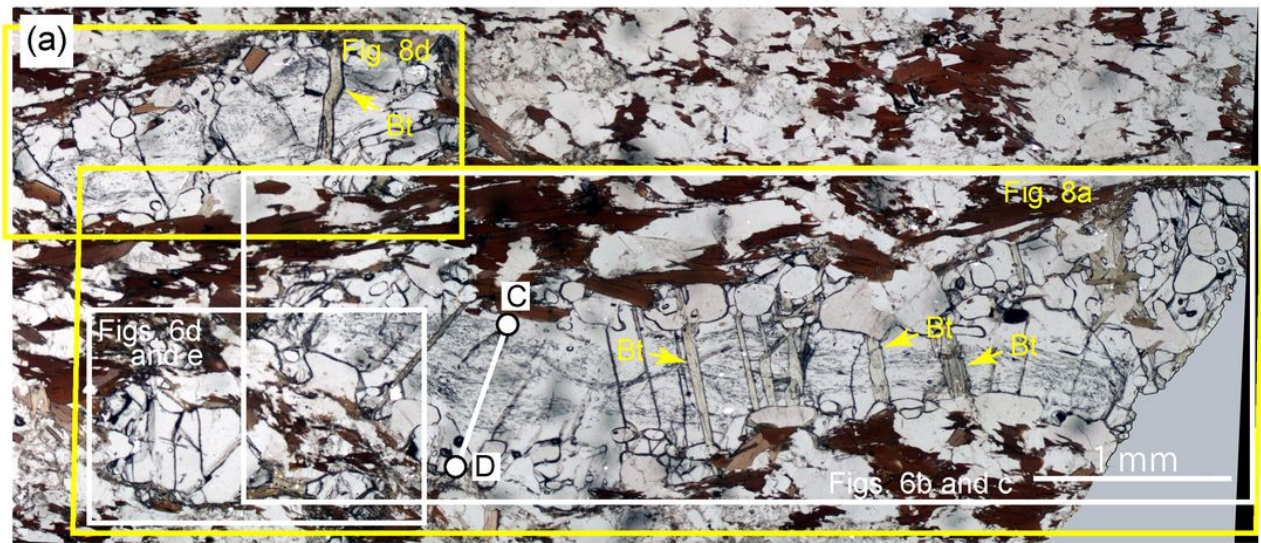


Figure 06 (Enami and others)

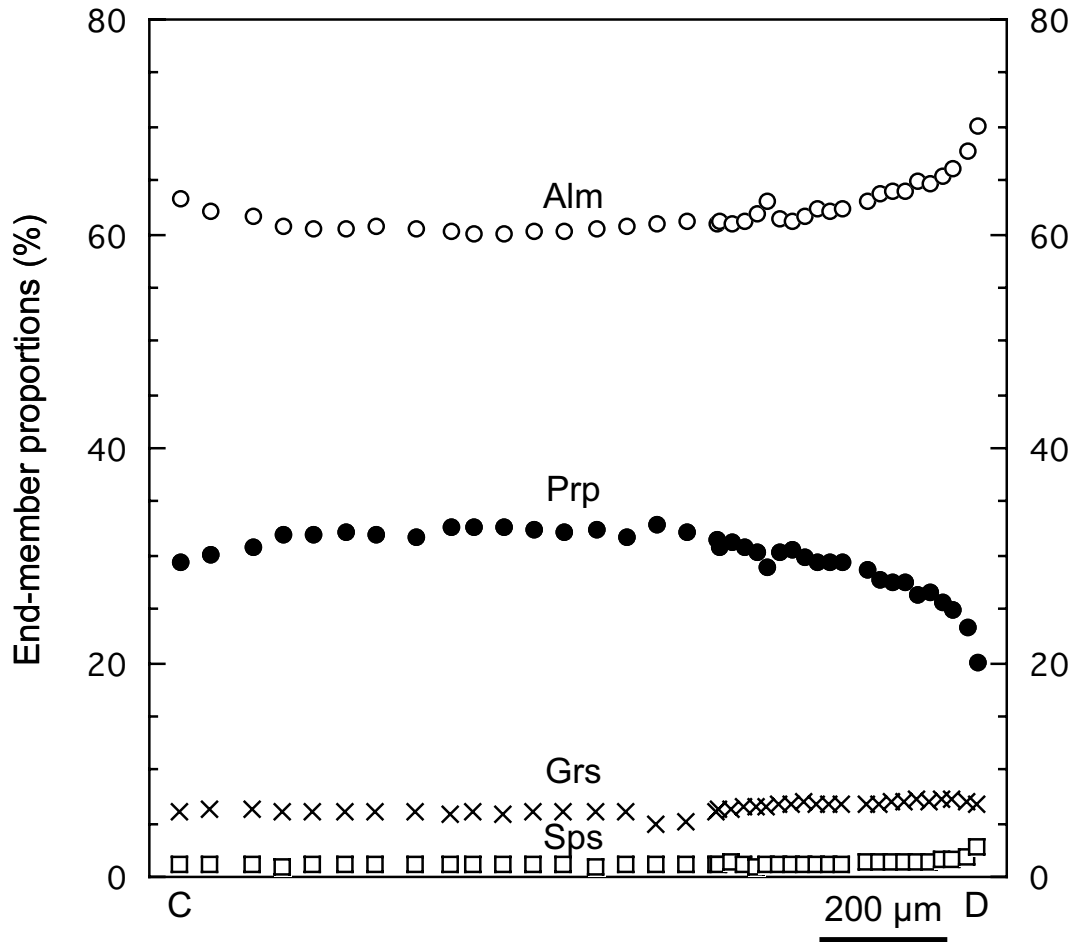


Figure 07 (Enami and others)

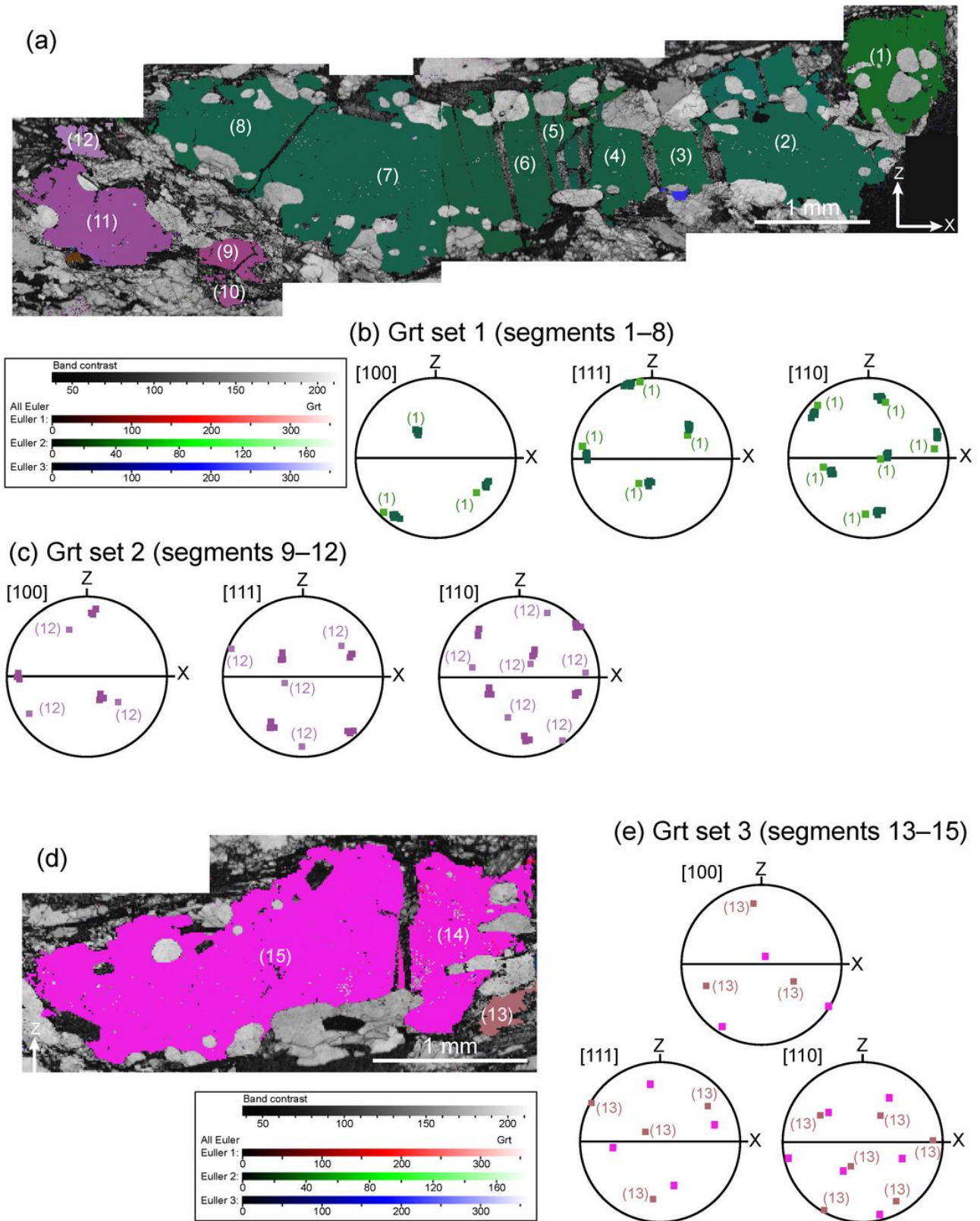


Figure 08 (Enami and others)

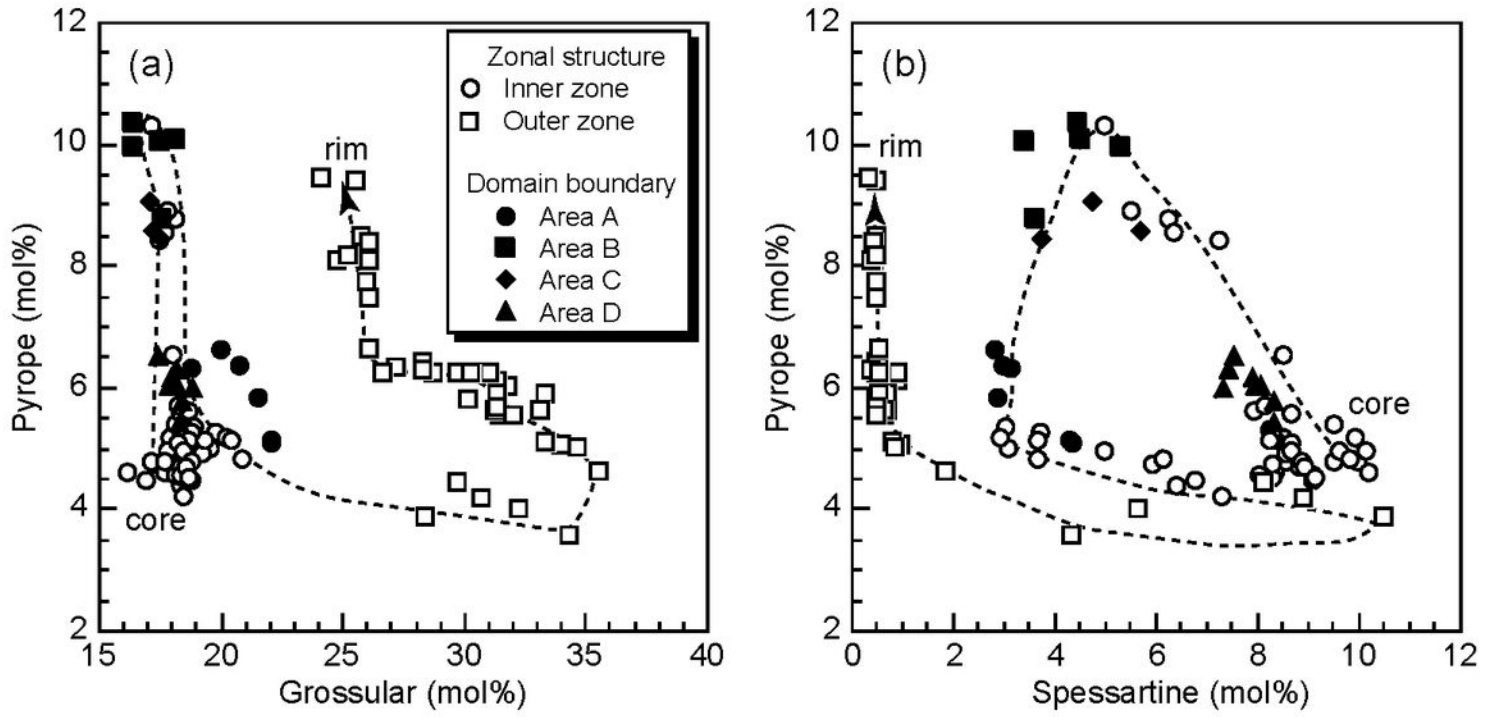


Figure 09 (Enami and others)

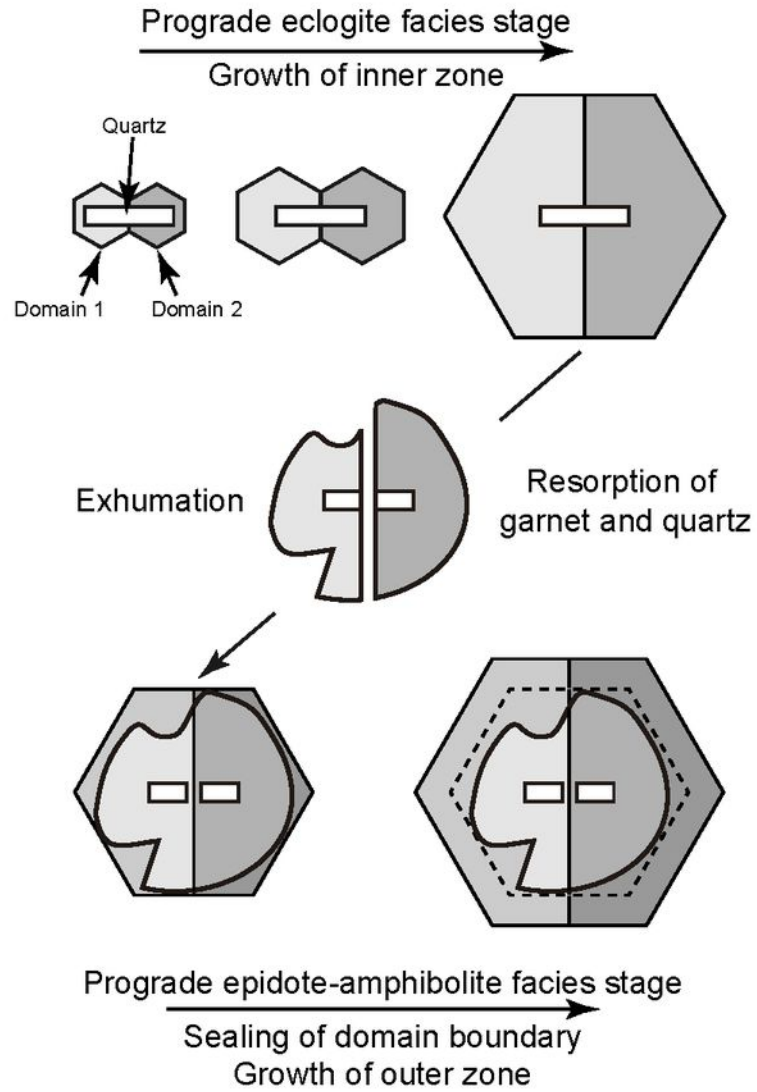


Figure 10 (Enami and others)